pp. 1–25 (2023)

Mathematical modelling for spatial optimization of irradiation during proton radiotherapy with nanosensitizers

M. Kuznetsov[a b] and A. Kolobov[b]

Abstract — A spatially distributed mathematical model is presented that simulates the growth of a non-invasive tumour undergoing treatment by fractionated proton therapy with the use of non-radioactive tumour-specific nanosensitizers. Nanosensitizers are injected intravenously before each irradiation to increase the locally deposited dose via a chain of reactions with therapeutic protons. Modelling simulations show that the use of nanosensitizers allows increasing treatment efficacy. However, their effect is restricted by the necessity of decreasing the energy deposited in tumour in order to comply to the normal damage restrictions. Normalization of tumour microvasculature that accompanies the treatment, also compromises nanosensitizers effect as it impairs their inflow in tumour. It is shown that spatial optimization of irradiation, with conservation of total dose deposited in tumour, can increase tumour cell damage for each single irradiation. However, eventually it may not lead to the overall increase of treatment efficacy, in terms of minimization of the number of remaining viable tumour cells, due to the influence of tumour cell repopulation between irradiations. It is suggested that an efficient way towards minimization of tumour cell repopulation may be the faster suppression of angiogenesis by eradication of metabolically deprived tumour cells. This method can be efficient even despite the fact that it would also cause the decrease of supply of nanosensitizers into the tumour.

Keywords: Mathematical oncology, numerical optimization, radiosensitizers, nanoparticles.

MSC 2010: 35Q92, 35Q93, 92C05

1. Introduction

Optimization of radiotherapy is a crucial problem in oncology, given its widespread use and applicability to the vast majority of tumours [24]. Increase of treatment efficacy can be achieved both by implementation of novel technologies into clinical practice and by rationalization of use of already implemented tools and techniques.

1.1. Novel technology: nanosensitizers for proton therapy

The most common form of radiotherapy involves delivery of radiation from a source located outside of the patient's body, mostly in form of photons, either X-rays or

[a]Department of Computational and Quantitative Medicine, Division of Mathematical Oncology, City of Hope, Duarte, CA 91010, USA

[b]Division of Theoretical Physics, P. N. Lebedev Physical Institute of the Russian Academy of Sciences, Moscow 119991, Russia. E-mail: scilpi@mail.ru

The reported study was funded by the Ministry of Science and Higher Education of the Russian Federation, subsiding agreement 075-15-2021-1347.

gamma rays. Although in clinical setting radiation is aimed to be focused on the tumour site, it inevitably affects all the tissues that it traverses. Despite the multiple technical achievements aimed at increasing the precision of tumour delineation by radiation [7], photon radiotherapy has severe limitations in its possible level of sparing normal tissues. This is especially pronounced for deeply located tumours, since the energy deposition density of a photon is maximal at the beginning of its path.

In contrast, protons deposit the majority of their energy at a specific depth, after which they come to a complete stop. This feature, discovered by William Henry Bragg as early as in 1903, holds for all charged particles [8]. The depth of the peak of energy release depends on the initial energy of protons. Therefore, proper combining of multienergetic proton beams can allow for precise tumour delineation. Overall, this results in a lower risk of development of adverse effects compared to traditional photon therapy.

One of the promising relevant technologies, aimed at the further reduction of side-effects during proton therapy, is the use of non-radioactive nanosensitizers that can be activated via nuclear reactions with protons. Ideally, they represent small volumes of the sensitizer covered by a layer of polymers with tumour-specific antibodies embedded in it. This allows for their targeted delivery to malignant cells. Radiosensitive elements, like boron, gold, and bismuth can lead to increase of the local dose under the influence of protons, due to emission of electrons and gamma quanta in result of nuclear reactions. Their products can be, in particular, alpha particles [3]. Since all of these particles have a range of only one to several cell diameters, this technique yields a localized increase of the absorbed dose in the targeted cells, further minimizing the damage to nearby normal tissues.

The efficacy of proton therapy with the use of nanosensitizers depends on multiple factors. Among them are successful delivery on nanoparticles to the tumour mass with their minimal-to-no accumulation in the surrounding normal tissues that would exacerbate their damage. Due to the dynamic nature of the penetration of particles from tumour microvasculature and of their specific binding and clearance from blood and tissues, the optimal timing of irradiation after their injection presents a non-trivial question.

Spatial redistribution of irradiation within the tumour also holds great capacity for optimization. In clinical practice, the uniform irradiation of tumour is generally pursued. However, it is well known that tumours predominantly bear non-uniform distribution of cells, which moreover possess different radiosensitivity. The latter in particular is determined by non-uniform oxygenation of cells and their heterogeneous cell cycle stage distribution. The latter, in its turn, influenced by the distribution of nutrients [55]. The presence of nanosensitizers should even more exacerbate the differential radiosensitivity of tumour cells. Due to the large size of nanosensitizers, comparable to the sizes of pores in the capillaries walls, it is reasonable to expect their penetration deep within tumour mass to be significantly hindered, which should result in their notably heterogeneous intratumoural distribution.

1.2. Rationalization of treatment: mathematical modelling

These problems can be investigated via mathematical modelling, in which a tumour and its microenvironment represent a single complex system, governed by differential equations. Mathematical modelling of this kind is a quickly developing field, which nowadays has led to several ongoing clinical trials (see, e.g., [1, 34, 41] for review). Optimization of temporal scheduling of medical interventions of different nature within a combined antitumour therapy is one of its major research topics [17, 30, 38].

The optimization of spatial distribution of irradiation has also been investigated by mathematical modelling. It has been proven rigorously that in case of a homogeneous tumour, the optimal distribution of radiation is also uniform [54]. A number of studies advocate the rationality of increasing the local dose in radioresistant, in particular hypoxic, areas [43, 47]. This result is undoubtedly correct for one potentially curative irradiation. However, the formulation of the corresponding problem for only one irradiation neglects dynamical alterations of distributions of viable tumour cells and their radiosensitivity during ongoing treatment. It is noteworthy that a straightforward attempt to perform dose boost in hypoxic tumour regions during the whole course of fractionated radiotherapy within a clinical trial in fact worsened the clinical outcome [53].

Another theoretical approach that stemmed from mathematical modelling and is referred to as 'spatiotemporally fractionated radiotherapy', suggests dividing tumour into several regions and delivering a high single fractional dose to each of them sequentially instead of irradiating the whole tumour volume each time [19, 52]. The authors of this approach demonstrated that with the precision inherent to the proton therapy it is possible to redistribute the dose within the tumour this way, along with keeping the normal tissue damage practically unaltered. The presence of setup uncertainties has also been integrated into their optimization algorithm [20]. However, this methodology assumes uniform cell radiosensitivity and uniform distribution of tumour cells. Moreover, in the corresponding works only static tumours were considered, with the dynamic aspects such as cell proliferation, tumour shrinking, and alterations of radiosensitivity and cell density fields being neglected. Partially this is justified by the fact that only short treatment protocols were considered in the corresponding works, consisting of no more than five fractions. The rationale behind this fact was that such spatiotemporal fractionation should be profitable for tumours that by themselves are generally treated with hypofractionation protocols (due to having low α/β ratio), and this method effectively creates additional degree of hypofractionation. While this methodology in our opinion holds great promise, it has not yet been tested in clinical setting.

The current work is built on our previous research in the field of optimization of radiotherapy and other antitumour treatments via mathematical modelling [27, 28, 31, 33, 36]. In particular, previously we have addressed the problem of spatial optimization of fractionated proton therapy [35]. We have suggested that in order to increase the overall tumour cell kill and therefore the probability of tumour cure, spatial redistribution of irradiation should accentuate regions

with sufficient amount of viable radiosensitive cells. In an idealized situation of a spherically-symmetrical tumour such regions are initially situated at the tumour rim. After damaging the cells in that regions, the optimization algorithm suggested that further irradiations should sequentially accentuate deeper located regions. That partially correlates with the abovementioned methodology of spatiotemporal fractionation. The key difference in the approaches, however, was that we did not assume tumours to have low α/β ratios. Moreover, we considered prolonged treatment with each part of the tumour eventually irradiated several times, and the first region to be irradiated was determined unambiguously, unlike in the mentioned approach [19]. Importantly, initial aiming of metabolically active populated areas was shown to promote faster penetration of nutrients in the tumour volume during the treatment. That led to faster proliferation of remaining cells, but also increased their radiosensitivity, rendering them an easier target for further irradiation. The feasibility of such reasoning at least for certain types of tumours is evidenced by the clinically observed phenomenon of accelerated tumour repopulation after several weeks of fractionated irradiation [56].

Recently, we have developed a model of proton therapy with the use of intravenously administered tumour-specific nanosensitizers [37]. We have shown that the efficacy of their use crucially depends on their size. On the one hand, its increase allows the nanoparticles to contain larger fraction of sensitizers. On the other hand, large size hinders their delivery in the tumour, with the critical process being the penetration of nanoparticles through the pores in the walls of tumour capillaries. Considering the physiologically plausible spectra of radii of capillary pores and the width of external polymer layer of nanoparticles of 7 nm, we suggested their optimal radius to be in the range of 13–15 nm.

This work represents the next step in investigating the problem of optimization of proton radiotherapy with the use of nanosensitizers. The paper is organized as follows. Section 2 presents the mathematical model of tumour growth and proton therapy with the use of intravenously administered nanosensitizers. In Subsection 3.1 one uniform irradiation without the use of nanosensitizers is considered. In Subsection 3.2 nanosensitizers are injected for a single subsequent irradiation, and the variation of injection timing and spatial optimization of irradiation are performed. Subsection 3.3 considers the whole course of fractionated proton therapy with nanosensitizers for both uniform and spatially optimized irradiations, and highlights the crucial issues that are expected to be met while introducing this approach into clinical practice. The discussion of the results in context of clinical setting is presented in Section 4.

2. Mathematical model

2.1. Equations

The block scheme of the main model interactions is presented in Fig. 1. The developed model contains 12 variables, which are the functions of the spatial and temporal coordinates r and t. The following system defines their dynamics:

$$
\begin{aligned}
&\text{proliferating tumour cells:} && \frac{\partial n_p}{\partial t} = \overbrace{Bn_p\cdot\Theta_p(\sigma)\frac{g}{g+g^*}}^{\text{proliferation}} \overbrace{-B\cdot[1-\Theta_{tr}(g)]n_p + B\cdot\Theta_{tr}(g)n_q}^{\text{transition}} \overbrace{-R_p}^{\text{irradiation}} \overbrace{-\frac{1}{r^2}\frac{\partial(I_s n_p r^2)}{\partial r}}^{\text{convection}};\\
&\text{quiescent tumour cells:} && \frac{\partial n_q}{\partial t} = \overbrace{B\cdot[1-\Theta_{tr}(g)]n_p - B\cdot\Theta_{tr}(g)n_q}^{\text{transition}} \overbrace{-\Phi(w)n_q}^{\text{starvation}} \overbrace{-R_q}^{\text{irradiation}} \overbrace{-\frac{1}{r^2}\frac{\partial(I_s n_q r^2)}{\partial r}}^{\text{convection}};\\
&\text{normal cells:} && \frac{\partial h}{\partial t} = \overbrace{-\frac{1}{r^2}\frac{\partial(I_s h r^2)}{\partial r}}^{\text{convection}};\\
&\text{damaged cells:} && \frac{\partial m}{\partial t} = \overbrace{R_p+R_q}^{\text{irradiation}} \overbrace{-Mm}^{\text{death}} \overbrace{-\frac{1}{r^2}\frac{\partial(I_s m r^2)}{\partial r}}^{\text{convection}};\\
&\text{interstitial fluid:} && \frac{\partial f}{\partial t} = \overbrace{[L_n c_n + L_a c_a]\cdot[p_c-p]}^{\text{inflow}} \overbrace{-L_l h p}^{\text{outflow}} \overbrace{+Mm+\Phi(w)n_q}^{\text{cell death}} \overbrace{-Bn_p\cdot\Theta_p(\sigma)\frac{g}{g+g^*}}^{\text{cell proliferation}} \overbrace{-\frac{1}{r^2}\frac{\partial(I_f f r^2)}{\partial r}}^{\text{convection}};\\
&\text{VEGF:} && \frac{\partial v}{\partial t} = \overbrace{S_v n_q}^{\text{secretion}} \overbrace{-\xi[c_n+c_a]v}^{\text{internalization}} \overbrace{-M_v v}^{\text{degradation}} \overbrace{+D_v\Delta v}^{\text{diffusion}};\\
&\text{normal capillaries:} && \frac{\partial c_n}{\partial t} = \overbrace{-M_c[n_q+m]c_n}^{\text{degradation}} \overbrace{+\frac{V_n v^*}{v+v^*}c_a}^{\text{normalization}} \overbrace{-\frac{V_d v}{v+v^*}c_n}^{\text{denormalization}} \overbrace{-\mu[c_n-1]\cdot\Theta(c_n-1)}^{\text{pruning}} \overbrace{-\frac{1}{r^2}\frac{\partial(I_s c_n r^2)}{\partial r}}^{\text{convection}};\\
&\text{abnormal capillaries:} && \frac{\partial c_a}{\partial t} = \overbrace{-M_c[n_p+k_M\{n_q+m\}]c_a}^{\text{degradation}} \overbrace{+\frac{Rv}{v+v^*}[c_n+c_a][1-\frac{c_n+c_a}{c_{\max}}]}^{\text{angiogenesis}} \overbrace{-\frac{V_n v^*}{v+v^*}c_a}^{\text{normalization}}\\
&&& \qquad \overbrace{+\frac{V_d v}{v+v^*}c_n}^{\text{denormalization}} \overbrace{+\frac{D_c}{r^2}\frac{\partial^2(gr^2)}{\partial r^2}}^{\text{active motion}} \overbrace{-\frac{1}{r^2}\frac{\partial(I_s c_a r^2)}{\partial r}}^{\text{convection}};\\
&\text{glucose:} && \frac{\partial g}{\partial t} = \overbrace{[P_n^g c_n + P_a^g c_a]\cdot[1-g]}^{\text{inflow}}\\
&&& \qquad \overbrace{-[\{\nu_g B\}n_p\Theta_p(\sigma) + Q_h^g\{n_q+h+n_p[1-\Theta_p(\sigma)]\}]\frac{g}{g+g^*}}^{\text{consumption}} \overbrace{+\frac{D_g}{r^2}\frac{\partial^2(gr^2)}{\partial r^2}}^{\text{diffusion}};\\
&\text{oxygen:} && \frac{\partial w}{\partial t} = \overbrace{P_w(c_n,c_a)[S(w_A)-S(w)]}^{\text{inflow}}\\
&&& \qquad \overbrace{-[\{\nu_w B\}n_p\Theta_p(\sigma) + Q_h^g\{n_q+h+n_p[1-\Theta_p(\sigma)]\}]\frac{w}{w+w^*}}^{\text{consumption}} \overbrace{+\frac{D_w}{r^2}\frac{\partial^2(wr^2)}{\partial r^2}}^{\text{diffusion}};\\
&\text{free nanoparticles:} && \frac{\partial u_f}{\partial t} = \overbrace{\{[L_n\gamma_n^u c_n + L_a\gamma_a^u c_a]\cdot[p_c-p]\}[u\cdot\Theta(p_c-p)+u_f\cdot\Theta(p-p_c)]}^{\text{convective inflow/outflow}}\\
&&& \qquad \overbrace{+[P_n^u c_n + P_a^u c_a]\cdot[u-u_f]}^{\text{diffusive inflow/outflow}} \overbrace{-\varkappa[n_p+n_q]u_f}^{\text{binding}} \overbrace{-L_l h p u_f}^{\text{lymphatic outflow}}\\
&&& \qquad \overbrace{-N_f}^{\text{reaction}} \overbrace{+\frac{D_u}{r^2}\frac{\partial^2(u_f r^2)}{\partial r^2}}^{\text{diffusion}} \overbrace{-\frac{1}{r^2}\frac{\partial(I_f u_f r^2)}{\partial r}}^{\text{convection}};\\
&\text{bound nanoparticles:} && \frac{\partial u_b}{\partial t} = \overbrace{\varkappa[n_p+n_q]u_f}^{\text{binding}} \overbrace{-N_b}^{\text{reaction}} \overbrace{-\frac{1}{r^2}\frac{\partial(I_s u_b r^2)}{\partial r}}^{\text{convection}};\\
&\text{solid stress:} && \sigma\equiv\sigma(s) = k\frac{[s-s_0][s-s_s]^2}{[1-s]^{0.1}}\cdot\Theta(s-s_s);\\
&\text{nanoparticles in blood:} && \frac{\partial u}{\partial t} = \overbrace{\textstyle\sum_{i=1}^{F}\delta(t-t_i)}^{\text{injections}} \overbrace{-Cu}^{\text{clearance}};\\
&\text{irradiations:} && R_x\equiv R_x(r,t) = \Gamma_x(u_b(r,t))\cdot\left[\textstyle\sum_{j=1}^{F}\delta(t-t_j)\right]\cdot n_x(r,t), \quad x=p,q;
\end{aligned}
\tag{2.1}
$$

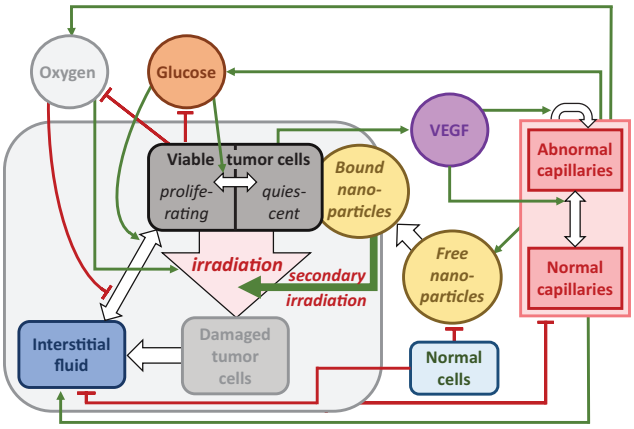

Figure 1. Scheme of the main interactions of the model governed by (2.1)–(2.2). Green arrows denote stimulating interactions, red lines show inhibiting interactions, white arrows correspond to the transitions of variables.

where

$$
\begin{aligned}
&s+f=1, \quad s=n_p+n_q+h+m\\
&\Theta_p(\sigma)=[1+\tanh(\varepsilon\{\sigma_p-\sigma\})]/2, \quad \Theta_{tr}(g)=[1+\tanh(\varepsilon\{g-g^*\})]/2\\
&\Phi(w)=\begin{cases}0, & w\geqslant w^*\\ M[\{w/w^*\}^2-2\{w/w^*\}+1], & w<w^*\end{cases}\\
&P_w(c_n,c_a)=P_w^0\cdot\frac{1.5[c_n+c_a]}{0.5+c_n+c_a}, \qquad S(w)=\frac{w^\chi}{[w^\chi+\widehat{w}^\chi]}\\
&f(I_f-I_s)=-K\frac{\partial p}{\partial r}, \qquad \frac{\partial p}{\partial r}=-\frac{\partial \sigma}{\partial r}\\
&\Gamma_x(u_b(r,t))=1-\exp(-k_x\{\alpha\cdot D(r,t)\cdot[\mathrm{OER}_\alpha(w(r,t))+K_u\cdot\{N_b(r,t)+N_f(r,t)\}]\\
&\qquad\qquad +\beta[D(r,t)\cdot\mathrm{OER}_\beta(w(r,t))]^2\}), \quad x=p,q\\
&N_y\equiv N_y(r,t)=[1-\mathrm{e}^{-\alpha_{\mathrm{NR}}\cdot D(r,t)}]\cdot\left[\textstyle\sum_{j=1}^{F}\delta(t-t_j)\right]\cdot u_y(r,t), \quad y=f,b\\
&\mathrm{OER}_y(w)=\frac{w\cdot\mathrm{OER}_y^{\max}+K_m}{w+K_m}, \quad y=\alpha,\beta.
\end{aligned}
\tag{2.2}
$$

The model considers spherically symmetric growth of a non-invasive tumour in normal tissue. Under sufficient supply of glucose g and oxygen w tumour cells reside in the proliferative state n_p, in which they increase their number exponentially with the use of interstitial fluid f as the source of mass. Under lack of glucose they transfer to the quiescent state n_q, this transition being reversible. When damaged by irradiation, proliferating and quiescent tumour cells transfer into damaged state m, in which they gradually die turning into interstitial fluid. Tumour cells are surrounded by normal cells h. All cells in total $s=n_p+n_q+m+h$ are considered as a porous solid phase fraction of the tissue. Interstitial fluid represents its second phase. It is able to flow in a viscous way through the pores within the solid fraction. The tissue is assumed to be saturated and incompressible, that is, the total density of cells and fluid is constant and normalized to unity.

The rate of cell proliferation depends on the rate at which they consume glucose and on the local solid stress $\sigma(s)$. The solid stress function is based on the assumption that the volume fraction of cells is linked with the average distance between them [40]. When the fraction of cells is normal, $s = s_0$, cell interactions result in zero solid stress. Cells brought close together tend to repel, while cells brought apart tend to attract until a certain intercellular distance is reached, at which interaction strength nullifies.

Interstitial fluid flows into the considered part of tissue from the capillaries. Two types of capillaries are considered: normal c_n and abnormal c_a. The latter have increased permeability to fluid, glucose and nanoparticles due to the influence of vascular endothelial growth factor, VEGF v. The action of VEGF also leads to angiogenesis, i.e., formation of new capillaries in abnormal state. VEGF is produced by nutrient-deprived quiescent cells and distributed by tissue via diffusion. At low VEGF concentrations capillaries normalize. Fluid drains into the lymphatic system, which is not considered explicitly, but it is assumed that its density is proportional to that of normal cells. Therefore, lymphatic capillaries are absent within the tumour. Blood capillaries also degrade within the tumour due to their rupture, implicitly caused by their displacement as well as chemical factors [21].

Glucose and oxygen flow from the capillaries into the tissue, diffuse through it, and are consumed by the cells. Proliferating tumour cells consume it much faster than the other types. For more detailed description of the mentioned aspects of the model we refer the reader to our previous work [37], as well as to our work [32], in which the used method of consideration of oxygen dynamics was introduced.

The damage of tumour cells due to irradiation is modelled by the modified version of the standard linear-quadratic equation, which determines the amount of cells surviving after a single irradiation with a given dose D [24]. The introduced modifications account for the three factors that affect the radiosensitivity of tumour cells. The first of them is oxygen effect, i.e., the fact that oxygenated cells are notably more radiosensitive than hypoxic cells. The second factor is increased radiosensitivity of proliferating cells compared to quiescent cells. These factors are accounted for in the way that was used in our work [33].

The third effect, which also can be effectively considered as the increase in cell radiosensitivity, is the deposition of additional dose in result of the chain of reactions with sensitizers, confined to nanoparticles located in immediate proximity to tumour cells. It is assumed to affect only the linear part of tumour cell radiosensitivity and to act independently of the oxygen effect. The nanoparticles penetrate into the tissue from blood via the processes of convection and diffusion through the pores in capillaries walls. They arrive in the considered part of tissue in a free state u_f, in which they diffuse passively through it and simultaneously move with the convective motion of the interstitial fluid. Nanoparticles are washed out via lymphatic system unless they specifically bind to tumour cells. In a bound state u_b they become immobilized relative to the tumour cells. When irradiated, both free and bound nanosensitizers are effectively spent on the increase of the effective dose deposited in tumour cells. The term of their expenditure is analogical to the term describing

the law of cell survival in result of irradiation.

There are two externally controlled variables in this model. One of them is time-dependent variable, which determines the concentration of nanoparticles in the blood $u(t)$. It increases instantaneously at the designated moments of time t_i. The second variable is, in general case spatially heterogeneous, dose of radiation $D(r,t)$, which is applied instantaneously at the specific moments of time t_j, F times during the treatment. In this work we consider quite standard temporal fractionation of radiotherapy, i.e., 30 irradiations administered during weekdays in 6 consecutive weeks. In the case of spatially uniform irradiation the used dose is $D_{st} = 1.8$ Gy, which is typical for a proton therapy fractionated in this manner. The moments of injection of nanosensitizers as well as the spatial distribution of irradiation are varied in search for more effective treatment schemes.

As the presence of free nanoparticles in the normal tissue increases its damage, we will demand the irradiations to satisfy the following constraint:

$$\begin{aligned}\left(\frac{\alpha}{\beta}\right)_h \cdot D \cdot [\mathrm{OER}_\alpha(w(r_T,t_j)) + K_u \cdot N_f(r_T,t_j)] + [D \cdot \mathrm{OER}_\beta(w(r_T,t_j))]^2 \\ = \left(\frac{\alpha}{\beta}\right)_h \cdot D_{st} \cdot \mathrm{OER}_\alpha(w(r_T,t_j)) + [D_{st} \cdot \mathrm{OER}_\beta(w(r_T,t_j))]^2 \quad \forall j \in [1,F]\end{aligned} \tag{2.3}$$

where r_T is the tumour radius and $(\alpha/\beta)_h$ is the alpha–beta ratio for normal tissue. In the case of uniform irradiation it results in the decrease of the used dose D. This constraint guarantees that the biologically effective dose administered to the normal tissue adjacent to the tumour border is kept the same as it would be in result of standard uniform irradiation without the use of nanosensitizers.

2.2. Parameters

The model contains several dozen parameters, which were estimated from the results of experiments of a different nature or, if that was impossible, were calibrated in order to reflect the known general features of tumour growth. The basic set of parameters is provided in Table 1, where the following normalization parameters are used to derive their model values: 1 h for time; 10^{-2} cm for length; $3 \cdot 10^8$ cells/mL for maximum cell density; $v = 10^{-11}$ mol/mL for VEGF concentration; 100 $\mathrm{cm}^2/\mathrm{cm}^3$ for capillary surface area density; 1 mg/mL for glucose concentration; 11 mM for oxygen concentration; 1 Gy for irradiation dose. The normalization factor for nanoparticle concentration is not used explicitly as it is linearly linked with the factor of dose enhancement by nanoparticles, K_u.

The choice of the majority of these model parameters is justified in our work [37]. The parameters governing nanoparticles diffusion and penetration from the capillaries are chosen for the nanoparticles with 13 nm radius, which in that work was shown to be close to optimal for the maximal tumour radiosensitization. The increased permeability of abnormal capillaries together with the absence of lymphatic outflow from the tumour mass allow reproducing the well-known phenomenon of enhanced permeability and retention of tumours, related to substances with high

Table 1. Model parameters.

Parameter	Description	Value	Based on
Cells:			
B	maximum rate of tumour cell proliferation	0.01	[18]
σ_p	critical stress for tumour cell proliferation	15	[40]
ε	smoothing parameter of Heaviside functions	500	[37]
M	maximum rate of death of tumour cells	0.01	[37]
Stress:			
k	solid stress coefficient	500	[37]
s_s	minimum fraction of interacting cells	0.3	[9]
s_0	normal fraction of cells	0.8	[9]
Interstitial fluid:			
L_n	hydraulic conductivity of normal capillaries	0.1	[49]
L_a	hydraulic conductivity of abnormal capillaries	0.22	[37]
p_c	fluid pressure in capillaries	4	[49]
L_l	hydraulic conductivity of lymphatic capillaries	1300	[49]
K	tissue hydraulic conductivity	0.1	[42]
VEGF:			
S_v	secretion rate	1	[26]
ξ	internalization rate	1	[39]
M_v	degradation rate	0.01	[29]
D_v	diffusion coefficient	21	[29]
Capillaries:			
R	maximum rate of angiogenesis	0.008	[15]
$c_{\max}$	maximum surface area density	5	[15]
M_c	degradation rate	0.03	[48, 15]
k_M	coefficient of degradation in the tumour core	2	[48, 15]
V_n	normalization rate	0.1	[16]
V_d	denormalization rate	0.1	[16]
μ	pruning rate	0.002	[32]
v^*	Michaelis constant for VEGF action	0.001	[37]
D_c	coefficient of active motion	0.03	[48, 15]
Glucose:			
g^*	Michaelis constant for consumption	0.01	[11]
P_n^g	permeability of normal capillaries	4	[14]
P_a^g	permeability of abnormal capillaries	10	[32]
ν_g	coefficient of proliferating tumour cells consumption rate	1200	[18]
Q_h^g	rate of consumption by normal cells	0.5	[4]
D_g	diffusion coefficient	100	[50]
Oxygen:			
w^*	Michaelis constant for consumption rate	0.005	[11]
P_w^0	inflow parameter	50	[46]
w_A	oxygen concentration in artery	5.87	[44]
$\widehat{w}$	concentration at which hemoglobin saturation is 50%	1.56	[13]
χ	Hill coefficient for oxygen-hemoglobin dissociation curve	2.55	[13]
Q_n^w	coefficient of proliferating tumour cells consumption rate	6400	[18]
Q_h^w	consumption rate by normal tissue	8	[4]
D_w	diffusion coefficient	720	[2]

Table 1. Model parameters (continuation).

Parameter	Description	Value	Based on
Irradiation:			
α	linear parameter of tumour cell radiosensitivity	0.3	see text
β	quadratic parameter of tumour cell radiosensitivity	0.03	[24] + see text
$(\alpha/\beta)_h$	alpha-beta ratio for normal tissue	3	[24]
$\mathrm{OER}_\alpha^{\max}$	maximum OER_α under aerobic conditions	2.4	[22]
$\mathrm{OER}_\beta^{\max}$	maximum OER_β under aerobic conditions	2.7	[22]
K_m	Michaelis constant for oxygen enhancement effect	0.193	[57]
k_q	coefficient of radiosensitivity of quiescent cells	0.2	[60]
K_u	factor of dose enhancement by nanosensitizers	5	see text
Nanoparticles:			
$\varkappa$	coefficient of binding with tumour cells	0.5	[37]
D_u	diffusion coefficient	5.0	[37]
C_u	clearance rate	0.09	[59]
γ_n^u	fraction of available pore cross-section area of normal capillaries	10^{-5}	[37]
γ_a^u	fraction of available pore cross-section area of abnormal capillaries	0.01	[37]
P_n^u	permeability of normal capillaries	0.001	[37]
P_a^u	permeability of abnormal capillaries	0.18	[37]
α_{NR}	coefficient of sensitizer expenditure in nuclear reaction	2	see text

molecular weights [58].

The radiosensitivity of tumour cells is chosen so that after the course of treatment the number of left viable tumour cells is of the order of hundreds. At that, the ratio of tumour cell radiosensitivity parameter α/β is typical for many tumour cell lines [24]. The expenditure of sensitizer in a nuclear reaction is set the way that it is close to saturation at $D = 1.8$ Gy. The factor of dose enhancement by sensitizer K_u is calibrated based on the preliminary findings of our experimental group, that show that the application of nanosensitizers can yield effective dose increase of about 30% in well-oxygenated conditions.

2.3. Numerical solution

During the numerical simulation of the system of equations (2.1)–(2.2), the equation for intercellular fluid was not considered explicitly due to the conservation law $f = 1 - s$. For the other variables, kinetic, diffusion and convection equations were solved sequentially at each time step. Kinetic equations were solved by the explicit Euler method. The use of this simple method is justified by the relative smallness of the used time steps that are required for the solution of convective equations. For diffusion equations, the implicit Crank–Nicholson scheme was used. These classical methods are described, e.g., in [45]. The convective equations were solved using the conservative flux-corrected transport algorithm with an implicit antidiffusion stage, introduced in [6]. This method by itself, however, introduces a small amount of uncorrectable diffusion, resulting in artificial invasion of tumour into the normal tissue. Modelling of normal tissue boundary is associated with similar problem. To over-

come it, two additional floating points were introduced on the computational grid, marking the positions of the tumour-normal tissue interface and of the normal tissue boundary. The coordinates of these points were calculated using the conservation of total cell volume when solving convection equations at each time step.

The following initial conditions were used, representing a spherical section of normal tissue of initial radius $r_0^N = 3$ mm with a small spherical colony of tumour cells of radius $r_0^T = 0.2$ mm located in its center, at $r = 0$:

$$\begin{cases} n_p(r,0) = s_{st} \\ h(r,0) = 0 \\ g(r,0) = 1\,, \\ w(r,0) = 1 \\ c_n(r,0) = 0 \end{cases} \quad r \leqslant r_0^T, \qquad \begin{cases} n_p(r,0) = 0 \\ h(r,0) = s_{st} \\ g(r,0) = 1\,, \\ w(r,0) = 1 \\ c_n(r,0) = 1 \end{cases} \quad r_0^T < r \leqslant r_0^N \tag{2.4}$$

$$n_q(r,0) = m(r,0) = v(r,0) = c_a(r,0) = u_f(r,0) = u_b(r,0) = u(0) = 0 \quad \forall r.$$

Here, s_{st} is the steady-state value for the fraction of cells. It differs from s_0 by less than a thousandth of a percent, which corresponds to a small stretching of the network of interconnected cells due to the pressure of fluid. The following boundary conditions were used:

$$\begin{aligned} \forall t \quad & \frac{\partial n_p}{\partial r}\Big|_0 = \frac{\partial n_q}{\partial r}\Big|_0 = \frac{\partial m}{\partial r}\Big|_0 = \frac{\partial h}{\partial r}\Big|_{r_0^T} = \frac{\partial v}{\partial r}\Big|_0 = \frac{\partial c_n}{\partial r}\Big|_0 = \frac{\partial c_a}{\partial r}\Big|_0 = \frac{\partial g}{\partial r}\Big|_0 \\ & = \frac{\partial w}{\partial r}\Big|_0 = \frac{\partial u_f}{\partial r}\Big|_0 = \frac{\partial u_b}{\partial r}\Big|_0 = 0 \\ & \frac{\partial n_p}{\partial r}\Big|_{r_0^T} = \frac{\partial n_q}{\partial r}\Big|_{r_0^T} = \frac{\partial m}{\partial r}\Big|_{r_0^T} = \frac{\partial h}{\partial r}\Big|_{r_0^N} = \frac{\partial g}{\partial r}\Big|_{r_0^N} = \frac{\partial w}{\partial r}\Big|_{r_0^N} = 0 \\ & v(r_0^N,t) = c_a(r_0^N,t) = u_f(r_0^N,t) = u_b(r_0^N,t) = 0,\ c_n(r_0^N,t) = 1. \end{aligned} \tag{2.5}$$

There are two separate convective motions in this model: $I_f = I_f(r,t)$ denotes the absolute convective velocity of the fluid, and $I_s = I_s(r,t)$ denotes the convective velocity of the solid phase. Summing up of the equations of dynamics of all cells and assuming both convective flow velocities to be zero at $r = 0$, equations (2.6) are obtained, which were used for defining convective velocities during numerical solution:

$$\begin{gathered} I_s = K\frac{\partial p}{\partial r} + \frac{1}{r^2}\int_0^r \{[L_n c_n + L_a c_a]\cdot[p_c - p] - L_l h[p - p_l]\} z^2 \mathrm{d}z \\ I_f = I_s - \frac{K}{f}\frac{\partial p}{\partial r}. \end{gathered} \tag{2.6}$$

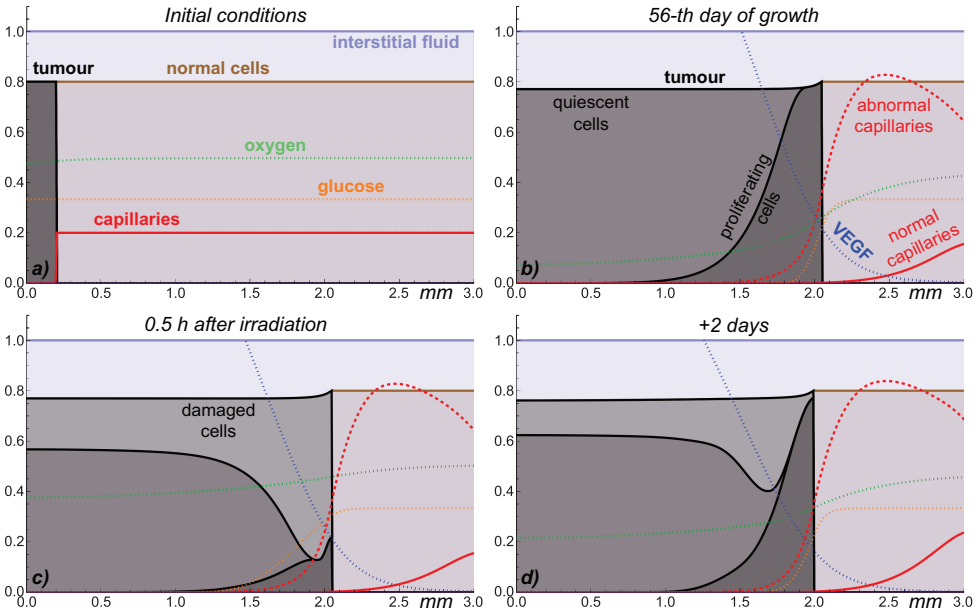

Figure 2. Distributions of model variables obtained from numerical simulations of free tumour growth and one uniform irradiation without the use of nanosensitizers. Values of the variables for glucose, oxygen, VEGF and capillaries are renormalized for better visualization.

3. Results

3.1. Free tumour growth and one irradiation without the use of nanosensitizers

Figure 2a shows the initial distributions of model variables. At this moment tumour consists entirely of proliferating cells, which number at first grows exponentially. However, already in several hours some tumour cells begin experiencing the deficiency of nutrients, supplied to the tumour mass from the surrounding capillaries. In result, tumour obtains the layered structure, with its inner core occupied mainly by quiescent cells, and the outer rim by proliferating cells. Such structure is typical for the tumour spheroids in experimental setting and for the non-invasive tumours *in vivo*. Nutrient deficiency is partially compensated by the initiation of angiogenesis, i.e., formation of new capillaries, stimulated by VEGF secreted by quiescent tumour cells. New abnormal capillaries have greater permeability which contributes to the increase of inflow of glucose to the tumour.

Figure 2b demonstrates the tumour and its microenvironment on the 56-th day of tumour growth. Despite ongoing angiogenesis, deep inside the tumour the capillaries are absent, which is consistent with the experimental observations [48]. Increased permeability of capillaries also results in enhanced inflow of fluid, which is not drained from the tumour due to the absence of lymphatic system therein. This leads to elevated fluid pressure inside the tumour, evidenced by the decreased local fraction of tumour cells across its volume compared to the fraction of normal

cells, which is maintained very close to the initial value. This qualitative feature also agrees with experimental data and has been previously reproduced in mathematical models [23].

Figure 2c corresponds to the moment about half an hour after the uniform irradiation of tumour with dose $D_{st} = 1.8$ Gy was performed. The resulting distribution of damaged cells highlights the heterogeneity of tumour cell radiosensitivity. Deep inside the tumour the cells resided in hypoxic non-proliferative state, and only about a third of them were damaged. However, close to the tumour rim as much as about 91% of proliferative normoxic cells transferred into the damaged state. Before the irradiation the concentration of tumour cells in the rim was elevated compared do deeper layers, since solid pressure becomes normalized at the tumour interface with normal tissue. Therefore, cell density at tumour rim remains elevated after a uniform irradiation. Moreover, it immediately starts increasing due to two reasons. The first and more prominent reason is the ongoing proliferation of tumour cells, which are now exposed to even greater levels of nutrients, since a large part of their active consumers were damaged. The second reason is the death of damaged cells accompanied by their transition into fluid and by its subsequent outflow from the tumour. Fluid outflow leads to tumour shrinkage which effectively compresses the cells at the tumour rim, overall contributing to the increase of their local density there. Figure 2d illustrates the outcome of tumour regrowth after two additional days in absence of further irradiations. Up to that moment tumour radius has decreased by almost 3% and has just begun to increase again due to the ongoing proliferation of tumour cells.

3.2. One irradiation with the use of nanosensitizers

Figure 3a summarizes the outcome of a single irradiation performed in different moments after a preliminary injection of nanosensitizers in blood on the same 56th day of tumour growth. Orange dots illustrate the case of standard uniform irradiation with $D_{st} = 1.8$ Gy without the use of nanosensitizers. It shows that as tumour grows, a single irradiation gradually becomes less efficient in terms of the resulting fraction of damaged tumour cells. This happens since the fraction of more radioresistant quiescent cells constantly grows in the tumour composition. These cells occupy the central part of tumour, while the more sensitive proliferative cells are constrained within a tumour rim, which width changes only slightly during the ongoing tumour growth.

3.2.1. Uniform irradiation with the use of nanosensitizers. Red dots in Fig. 3a show the fraction of damaged tumour cells due to same uniform irradiation but with the use of nanosensitizers. At the first hours, when the concentration of nanosensitizers in blood is high, they actively flow into the tumour, increasing its effective radiosensitivity and compensating for the increase of the pool of its quiescent cells. The maximum fraction of potentially damaged tumour cells is achieved about one day after the injection of nanosensitizers. After that due to the clearance of nano-

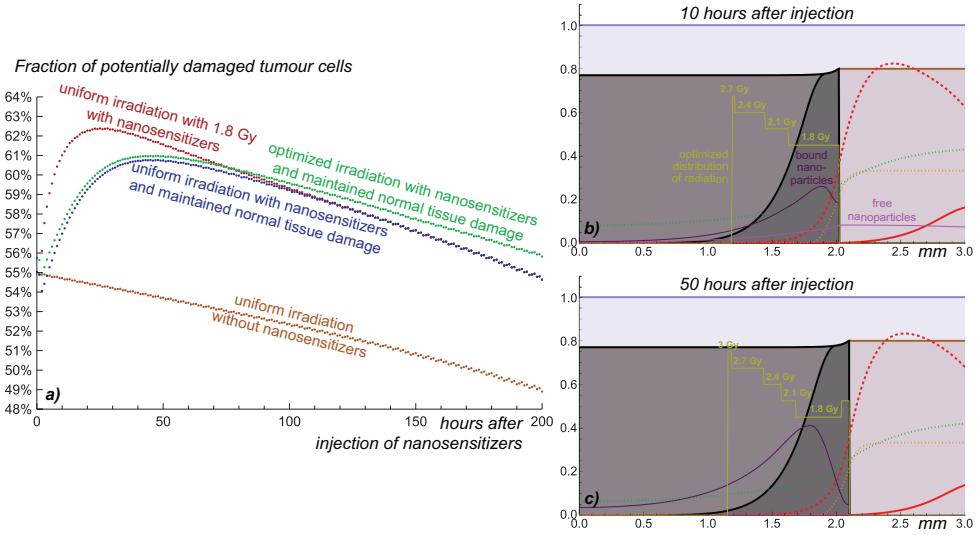

Figure 3. a) Dynamics of the fraction of potentially damaged tumour cells after a single injection of nanosensitizers at the 56th day of tumour growth. b,c) Distributions of model variables 10 and 50 hours after nanosensitizers injection. Yellow lines correspond to optimized distribution of radiation with normal tissue damage maintained at the level of standard treatment without nanosensitizers. Meaning of unlabelled lines corresponds to that in Fig. 2.

particles from the body their inflow in tumour gradually drops down to negligible values.

As nanoparticles penetrate in the tissue, the concentration of their unbound form in normal tissue also initially rises. Thus, a uniform irradiation with standard dose of 1.8 Gy during this period would lead to greater normal tissue damage, and overall to greater toxicity, than during the standard treatment without nanosensitizers. In order to maintain normal tissue damage at the standard level, the used uniform dose should be decreased. According to (2.3) introduced above, the corresponding uniform dose falls down to ≈ 1.58 Gy 10 hours after the nanosensitizers injection. After that it effectively returns to its original level at the span of about four days. Blue dots in Fig. 3a correspond to the case of uniform irradiation with adjusted doses and therefore with maintained normal tissue damage. Right after the injection of nanosensitizers such irradiations are even less efficient than the standard uniform irradiation without the use of nanosensitizers. It is so due to the fact that initially the level of free nanosensitizers in the normal tissue starts increasing rapidly, but only a very small amount of them penetrates the tumour and binds to the tumour cells. Fast accumulation of nanosensitizers in the tumour is prevented by two factors. One of them is the scarcity of capillaries inside the tumour. Another is the partial washout of nanosensitizers from the tumour by convective flow of the fluid, which has elevated pressure inside the tumour. For the used parameter set, the uniform irradiation with the use of nanosensitizers and maintained normal tissue damage is the most effective about two days after the nanosensitizers injection. It allows increasing the

fraction of damaged cells by additional 6% compared to the case of tumour irradiation at the 56th day of its growth.

3.2.2. Spatially optimized irradiation. The optimization of spatial distribution of irradiation was performed with the goal of increasing the resulting fraction of damaged tumour cells along with maintaining normal tissue damage at the acceptable standard level. For the mathematical tractability we have used the assumption that such dose distributions should deposit equal total energy over the whole tumour volume. This is justified by the localized nature of energy deposition by protons in tissue. In particular, the dose in the entrance region of a proton beam is largely independent of the beam range. Such justification has been used previously in similar optimization studies [51].

The procedure of spatial optimization was performed in a rather straightforward way. The computational grid elements, in which tumour cells were located, were sorted by their potential efficiency. It was defined as the concentration of newly damaged tumour cells $R_p + R_q$ in a grid element after its localized irradiation with a small dose dD. After increasing the local dose in a grid element its efficiency was recalculated as the additional concentration of damaged tumour cells after the dose increase by dD. Eventually the efficiency of each grid element decreased with the gradual dose increase. The algorithm boiled down to the iterative choosing of the most efficient grid element and to increasing the dose in it until it stopped being the most efficient. This was performed until the total energy deposited in the tumour reached the predefined level. Overall this led close to maximization of the integral number of damaged tumour cells over the whole tumour volume, this measure being proportional to $\int_0^{r_T} [R_p(r) + R_q(r)] r^2 \, \mathrm{d}r$.

However, due to the nonlinear nature of dose-effect relation in (2.1), under using of sufficiently small values of dD the efficiency of each grid element could initially increase with the gradual dose increase. In this case the whole algorithm resulted in notably suboptimal distributions of irradiation, which could occasionally even be less efficient than its uniform distribution. It was checked that the use of the dose portion as high as $dD = 0.3$ allowed to avoid this outcome always leading to optimized distributions of irradiation.

Two examples of spatially optimized distributions are shown in Figs. 3b and 3c for the moments of 10 and 50 hours after the injection of nanosensitizers. After 10 hours still a notable level of free nanoparticles persists in the normal tissue, therefore the total energy deposited in tumour is less in this case. As the figure shows, the optimal distribution of irradiation covers the most radiosensitive area of tumour. The local dose rises towards the tumour center, where cell radiosensitivity decreases. After 50 hours this qualitative picture is mostly maintained, however, at the very tumour rim a small local increase in dose is also suggested. This is explained by the fact that up to this moment the peak of concentration of bound nanoparticles, which are immobilized with respect to tumour cells, has effectively moved deeper in the tumour mass. The tumour rim is gradually repopulated by newborn tumour cells with notably decreased amount of bound nanoparticles, since

at this moment the rate of their inflow from blood is already very low.

Green dots in Fig. 3a correspond to the efficiency of such spatially optimized irradiations. As they show, the spatial optimization provides only minor increase of efficiency of a single irradiation. It yields additionally only $\approx 1.2\%$ of increase in fraction of potentially damaged tumour cells compared to the uniform irradiation with nanosensitizers at 50 hours after their injection.

3.3. Whole course of treatment

For the consideration of the whole course of fractionated proton therapy, we fixed the time interval between an injection of nanosensitizers and a consequent irradiation as 23 hours. This was done on the basis that, firstly, the frequent optimization of this time interval in clinical setting is a quite impossible task. Secondly, the previous section showed that the formal optimal interval can be notably greater than one day, which is already a standard interval between the fractions of irradiation. In light of this, 23 hours interval seems reasonable from a clinical point of view, as an injection can be administered right after a previous irradiation has been performed, when a patient still stays in a medical facility.

3.3.1. Uniform irradiation. Figure 4 summarizes the outcome of the whole course of radiotherapy in standard case, i.e., without the use of nanosensitizers (orange lines), as well as with their use in two cases: with keeping the standard irradiation dose of 1.8 Gy (red lines) and with maintaining normal tissue damage at acceptable standard level (blue lines). The figure shows that the use of nanosensitizers provides only moderate increase of treatment efficiency. The number of viable tumour cells left after the standard treatment is ≈ 849, while the use of nanosensitizers with maintained normal tissue damage allows reducing it to ≈ 519. The dynamics of tumour cell radius as well does not change significantly. From the point of view of tumour regrowth the use of nanosensitizers allows gaining only about 60 hours in terms of the number of viable cells and 70 hours in terms of tumour radius.

The modesty of this result is due to the relative weakness of the effect of nanosensitizers by themselves and due to the necessity of decreasing the energy deposited in tumour in order to comply to normal damage restrictions. Maintaining the standard dose allows decreasing the minimal number of viable tumour cells down to ≈ 312, which is slightly more than the third of those left after the standard treatment without nanosensitizers. Another factor that contributes to poor increase of treatment efficacy is the normalization of capillaries structure and density during the course of therapy. While the cells are actively eradicated, the amount of VEGF that they secrete falls down drastically and the microvasculature tends to return to its normal state. Therefore it becomes increasingly difficult for the nanosensitizers to penetrate into the tumour mass. This is illustrated by the graphs of the relative amount of nanosensitizers in blood, which maintain their shape from week to week, and on viable tumour cells. The latter decreases as treatment goes despite the fact that the very number of the viable tumour cells falls down. In case of irradiation with

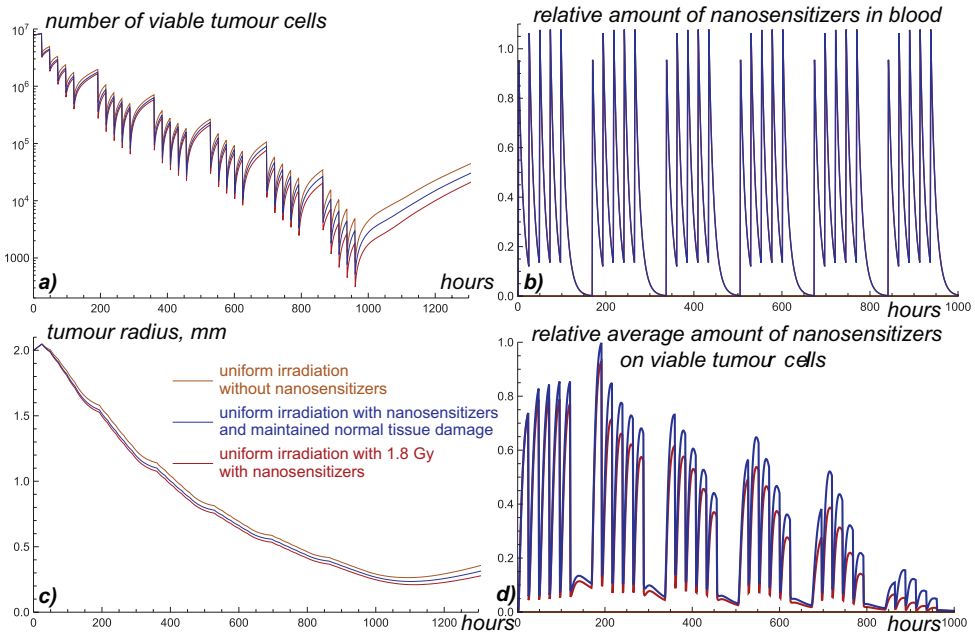

Figure 4. a) Number of viable tumour cells, b) relative number of nanosensitizers in blood, c) tumour radius, and d) relative average number of nanosensitizers on viable tumour cells during proton therapy courses with uniform irradiation under designated conditions.

standard dose of 1.8 Gy this effect is more pronounced since initial faster killing of tumour cells leads also to greater suppression of VEGF production.

3.3.2. Spatially optimized irradiation aimed at increase of tumour cell damage. Figure 5 illustrates the course of proton therapy with the use of nanosensitizers and optimized distribution of irradiation maintaining the normal tissue damage at the standard acceptable level. The first fraction of optimized irradiation is close to the ones depicted above in Fig. 3, and it accentuates tumour rim with the most radiosensitive cells. This leads to the fact that at the moment of the second fraction, illustrated in Fig. 5a, the outer part of tumour contains more damaged and less radiosensitive viable cells. Therefore, it becomes reasonable to increase the local dose within the tumour core. The killing of cells there is moreover now facilitated by the accumulation of nanosensitizers supplied by already two intravenous injections. However, notable repopulation of cells at the tumour rim also demands redistribution of part of energy towards it.

Each of the subsequent fractions as well has to focus partially on the tumour rim in order to compensate for the tumour cell repopulation. The rest of energy is effectively alternated between outer and inner tumour parts, as the plots for the third and fourth fractions of radiation show. Along the course of treatment the tumour mass shrinks significantly, and the pattern of alternation of irradiated zones gradually weakens. As it is shown, the difference between 19th and 20th irradiations is

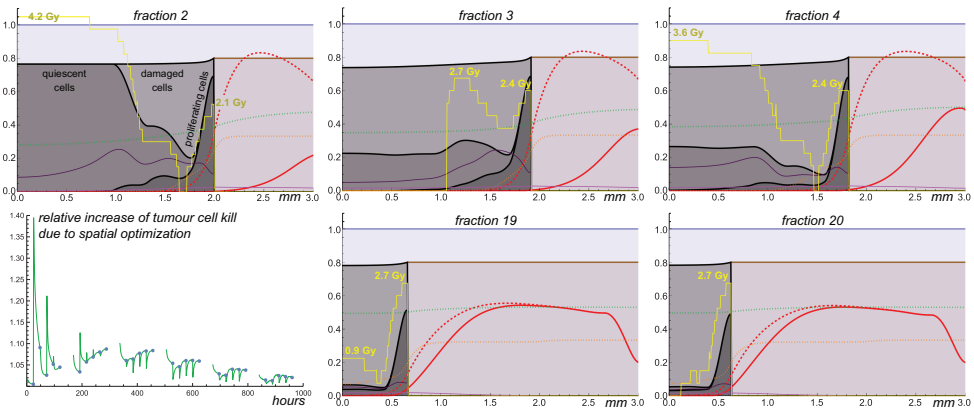

Figure 5. Optimized spatial distribution of irradiations for fractions 2, 3, 4, 19, and 20. Meaning of unlabelled lines corresponds to that in Fig. 2. The bottom left plot shows relative increase of efficiency achieved by spatial redistribution of irradiation, in terms of tumour cell kill.

not so prominent and the optimized spatial distributions of radiation mainly correlate with the distribution of proliferating cells.

The bottom left figure shows the efficiency of each of the spatially optimized irradiations. The efficiency is measured in terms of instantaneous tumour cell kill, in relation to the uniform irradiations that would be performed at the same moments of time. The dots denote the actual moments of irradiations, while the lines correspond to interpolations that rely on constantly updated spatially optimized irradiations. This plot reflects the complex dynamics taking place in the model. It is in particular affected in nontrivial way by the injections of nanosensitizers happening 23 hours before each irradiation, which for the majority of them is one hour after the previous irradiation. The graph confirms that each of the used optimized irradiations indeed leads to greater tumour cell kill than the uniform ones.

Nevertheless, somewhat counterintuitevely, the whole course utilizing optimized distributions of irradiation turns out to be less efficient than the whole course of standard proton therapy with, and even without, the use of nanosensitizers. This is illustrated by the green line in Fig. 6a, which shows the relative numbers of viable tumour cells during the treatment, with respect to the standard proton therapy without nanosensitizers. At the end of treatments the ratio of the remaining viable tumour cells is more than 2.2 for them. Blue line depicts the above-discussed treatment with nanosensitizers and uniform irradiations maintaining normal tissue damage.

The reason for this seeming contradiction lies in the fact that such optimization of radiation distribution does not account for the repopulation of tumour cells, taking place between irradiations. Therefore, the dynamics of cells between fractions may, and eventually does, override the gained increase in tumour cell kill.

3.3.3. Spatially optimize irradiation accentuating proliferative or quiescent cells. One straightforward way to compensate for the tumour cell repopulation

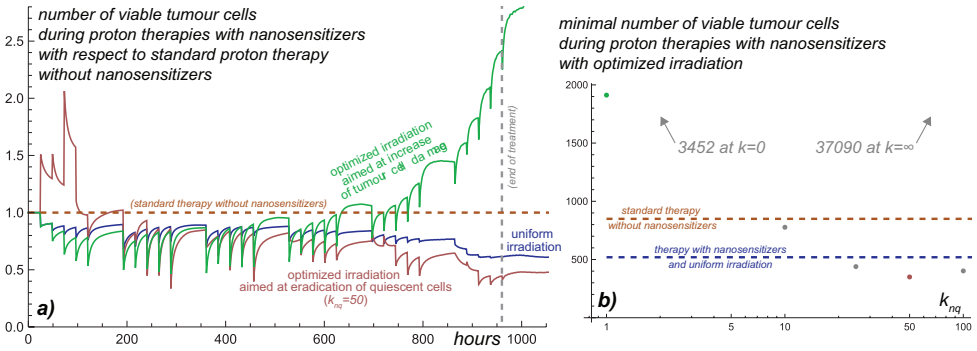

Figure 6. a) Dynamics of viable tumour cell numbers during designated proton therapies with nanosensitizers, with respect to the standard proton therapy without nanosensitizers. b) Minimal numbers of viable tumour cells during proton therapies with nanosensitizers with optimized irradiation, depending on the coefficient of accentuation of areas populated by quiescent cells, k_{nq}.

is to find the irradiation distribution that would provide the minimal number of viable tumour cells at the moment of the next irradiation. However, the realization of a corresponding algorithm would require frequent recalculations of tumour growth dynamics, dramatically increasing the computational costs. Moreover, it still will not guarantee the minimization of the final number of viable tumour cells since the alterations of earlier irradiations would affect the tumour dynamics during the whole remaining course of treatment (as the following results will prove).

In attempt to optimize the efficacy of the whole treatment by the decisions based each time only on the current knowledge of the model state, we have altered the objective function for optimization as follows:

$$\int_0^{r_T} [R_p(r) + k_{nq} \cdot R_q(r)] r^2 \, \mathrm{d}r$$

where k_{nq} can be referred to as the coefficient of accentuation of areas populated by quiescent cells. The above discussed case thus corresponds to $k_{nq} = 1$. The numbers of tumour cells at the end of optimized treatments corresponding to its different values are provided in Fig. 6b.

Interestingly, as this figure shows, a mere accentuation of irradiation only on the areas populated by currently proliferating tumour cells, corresponding to $k_{nq} = 0$, only exacerbates the effect of tumour cell repopulation. This is due to the fact that in the model their damage rapidly leads to the decrease of their rate of glucose consumption. This allows glucose to penetrate deeper in the tumour volume and leads to the transition of quiescent cells into proliferative state and thus their active repopulation.

Expectedly, the extreme opposite case, formally corresponding to $k_{nq} = \infty$, yields even much worse result, as it completely ignores the areas populated by currently proliferating, but not quiescent, tumour cells. However, initial increase of the value of k_{nq}, starting from zero, does lead to the increase of treatment efficacy, approximately until k_{nq} reaches the value of 50. The pink line in Fig. 6a corresponds

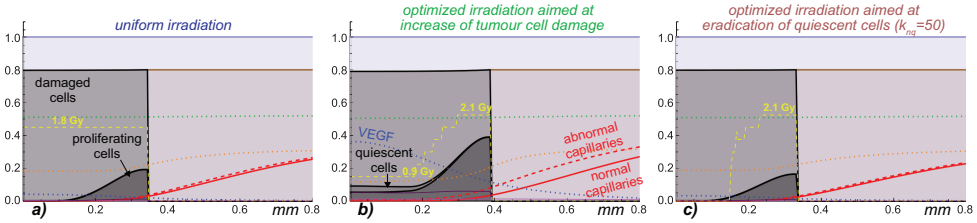

Figure 7. Distributions of model variables at the moment of the 28th fraction of irradiation for the designated types of proton therapy with the use of nanosensitizers. Yellow lines correspond to the distributions of radiation, with normal tissue damage maintained at the level of standard treatment without nanosensitizers. Meaning of unlabelled lines corresponds to that in Fig. 2.

to the therapy with this value of it. However, even such treatment allows to decrease the final number of viable tumour cells by a factor of only ≈ 1.5 compared to the treatment with uniform irradiation and the use of nanosensitizers.

The reasons for efficiency of accentuation of the areas populated by quiescent cells can be explained via Fig. 7. It shows the distributions of the model variables close to the end of treatments, at the moment of the 28th fraction of radiation, for the cases where its spatial distribution is: a) uniform; b) aimed at maximization of the instantaneous tumour cell kill ($k_{nq} = 1$); c) aimed at eradication of quiescent cells, with $k_{nq} = 50$, which is the most optimal of the discussed cases. Crucially, as Fig. 7c shows, such great value of k_{nq} by itself does not mean that the areas populated by proliferating cells are avoided. To the end of the therapy, when the vast majority of quiescent cells are already eliminated, the areas where they are left largely overlap with the ones occupied by proliferating cells. That results in the depicted distribution of irradiation, focused on the tumour rim.

The major difference that distinguishes the treatment, aimed at maximization of instantaneous tumour cell kill, illustrated in Fig. 7b, is the significant amount of abnormal capillaries. Their permeability for glucose is 2.5 times higher, that that of the normal ones. Therefore, ongoing angiogenesis allows this tumour to maintain notably larger tumour cell population. At that, the ultimate reason for the continuation of angiogenesis in this case is the presence of significant population of quiescent cells in the tumour core. These cells continue to secrete sufficient amounts of pro-angiogenic factor VEGF that eventually leads to the increase of tumour supply with nutrients (see Fig. 1 to recall the interaction of the model variables).

Such situation is the outcome of the fact that the maximization of instantaneous tumour cell kill focuses predominantly on the proliferating tumour cells as the most radiosensitive ones. In other depicted cases, with uniform irradiation and $k_{nq} = 50$, the level of ongoing angiogenesis is almost negligible and it leads to notably smaller volumes of the corresponding tumours. Notably, this happens despite the reduced supply of nanosensitizers to these tumours, which is visible from these figures.

4. Discussion

The presented study highlights the problems that can be expected for a proton therapy with the use of tumour-specific non-radioactive nanosensitizers. With the currently experimentally estimated increase in irradiation efficiency that they can provide, the study suggests that their overall input in the increase of the whole treatment efficacy can be rather moderate. Modelling shows that their action *in vivo* can be notably compromised by their restricted inflow into tumour through the microvasculature, located mainly outside the tumour mass. Its effective permeability surface area product is moreover expected to significantly decrease during the treatment in result of cessation of tumour-induced angiogenesis, which should especially affect the later fractions of radiation. Another reason for the restriction of efficacy is the necessity to maintain a tolerable level of damage of normal tissue. Free nanoparticles will also penetrate in it after their injection, with notable amount remaining there up to the moment of the consequent irradiation.

As it was discussed in Section 1, spatial optimization of irradiation is a topic currently gaining considerable attention in the literature, with different approaches having been suggested. This study brings up an important concern to this topic, as it shows that the increase in the tumour cell kill for each single irradiation may not convert to the overall increase of treatment efficacy. Therefore, the influence of tumour cell repopulation between irradiations also has to be accounted for. It is suggested that the efficient way towards minimization of tumour cell repopulation should be the faster suppression of angiogenesis. In the presented model this can be achieved by faster eradication of metabolically deprived tumour cells. Such approach was shown to result in more efficient treatment, even despite the accompanying decrease of the supply of nanosensitizers into the tumour. Therefore, the decrease of tumour cell carrying capacity by cessation of angiogenesis can be a more effective strategy for treatment optimization than the increase of tumour cells exposure to nanosensitizers. Notably, the effect of angiogenesis on tumour carrying capacity has been previously highlighted in mathematical modelling works starting from the pioneers of research of tumour angiogenesis [25].

It should be noted that this study was conducted with the simulations of a rather small tumour. It can be expected that larger and more heterogeneous tumours can be more respondent to optimized spatial irradiations, especially in the case of containing large necrotic areas. Our previous work clearly speaks in favor of this idea [35].

Although this study raises important concerns for the clinics, the suggestion of specific recommendations for the practical use lies outside of its scope. One reason for that is yet insufficient body of experimental data on the effect of nanosensitizers. Moreover, there is currently no experimental data on their combination with the other effects leading to differential tumour cell radiosensitivity. In this work quite phenomenological approach was used to account for it. Another reason is that in order to produce useful practical suggestions an extensive investigation has to be performed. Importantly it should account for all the uncertainties associated with determining the underlying dynamics governing tumour development, defining the corresponding model parameters and their reaction to external influences, as well as

accounting for the errors in tumour delineation and patient positioning. To continue this line of reasoning, the current study also has not accounted for tumour genetic heterogeneity, host immune response, microvessel destruction by irradiation, possible deceleration of cell cycle in response to irradiation, among other nontrivial effects. In addition, the changes of tumour cell metabolism in response to radiation damage were also accounted for in a phenomenological way, due to the lack of the relevant data in the literature. Summing up, as it is always the case in biomathematics, life constantly turns out to be much more complicated that any modelling can suggest. Therefore, it can be envisioned that valid practical suggestions should remain robust under substantial perturbations of the underlying model dynamics.

This being said, it can be expected that the optimized schemes involving non-uniform irradiation should nevertheless involve periodic accentuation of populated radiosensitive zones. In our current work such method manifested itself even when using the large values of the coefficient of accentuation of areas populated by quiescent cells. In clinical setting the promising and quite elaborated relevant option to be used can be targeting the tumour regions, most active in FDG-PET scans, that should correlate with such zones. It is intriguing that certain recent clinical results [5] show the potential of such approach for head and neck cancer in case of sufficiently frequent update of tumour form and composition.

References

1. P. M. Altrock, L. L. Liu, and F. Michor, The mathematics of cancer: integrating quantitative models. *Nature Reviews Cancer* **15** (2015), No. 12, 730–745.
2. C. Androjna et al., Oxygen diffusion through natural extracellular matrices: implications for estimating 'critical thickness' values in tendon tissue engineering. *Comparative Biochemistry and Physiology, part A: Physiology* **14** (2008), No. 4, 559–569.
3. M. Azarkin, M. Kirakosyan, and V. Ryabov, Study of nuclear reactions in therapy of tumours with proton beams. *International Journal of Molecular Sciences* **24** (2023), No. 14.
4. P. G. B. Baker and R. F. Mottram, Metabolism of exercising and resting human skeletal muscle, in the post-prandial and fasting states. *Clinical Science* **44** (1973), No. 5, 479–491.
5. D. Berwouts et al., Long-term outcome of 18F-fluorodeoxyglucose-positron emission tomography-guided dose painting for head and neck cancer: matched case-control study. *Head & Neck* **39** (2017), No. 11, 2264–2275.
6. J. P. Boris and D. L. Book, Flux-corrected transport. I. SHASTA, a fluid transport algorithm that works. *Journal of Computational Physics* **11** (1973), No. 1, 38–69.
7. T. Bortfeld, IMRT: A review and preview. *Physics in Medicine & Biology* **51** (2006), No. 13, R363.
8. A. Brown and H. Suit, The centenary of the discovery of the Bragg peak. *Radiotherapy and Oncology* **73** (2004), No. 3, 265–268.
9. H. Byrne and L. Preziosi, Modelling solid tumour growth using the theory of mixtures. *Mathematical Medicine and Biology: A Journal of the IMA* **20** (2003), No. 4, 341–366.
10. F. P. Cammarata et al., Proton boron capture therapy (PBCT) induces cell death and mitophagy in a heterotopic glioblastoma model. *Communications Biology* **6** (2023), No. 1, 388.
11. J. J. Casciari, S. V. Sotirchos, and R. M. Sutherland, Mathematical modelling of microenvir-

onment and growth in EMT6/Ro multicellular tumour spheroids. *Cell Proliferation* **25** (1992), No. 1, 1–22.

12. G. A. P. Cirrone et al., First experimental proof of Proton Boron Capture Therapy (PBCT) to enhance protontherapy effectiveness. *Scientific Reports* **8** (2018), No. 1, 1141.
13. T. Clerbaux et al., Comparative study of the oxyhaemoglobin dissociation curve of four mammals: man, dog, horse and cattle. *Comparative Biochemistry and Physiology, Part A: Physiology* **106** (1993), No. 4, 687–694.
14. G. Clough and L. H. Smaje, Exchange area and surface properties of the microvasculature of the rabbit submandibular gland following duct ligation. *The journal of Physiology* **354** (1984), No. 1, 445–456.
15. P. V. Dickson et al., Bevacizumab-induced transient remodeling of the vasculature in neuroblastoma xenografts results in improved delivery and efficacy of systemically administered chemotherapy. *Clinical Cancer Research* **13** (2007), No. 13, 3942–3950.
16. R. P. M. Dings et al., Scheduling of radiation with angiogenesis inhibitors Anginex and Avastin improves therapeutic outcome via vessel normalization. *Clinical Cancer Research* **13** (2007), No. 11, 3395–3402.
17. A. dOnofrio et al., On optimal delivery of combination therapy for tumors. *Mathematical Biosciences* **222** (2009), 13–26.
18. J. Freyer and R. Sutherland, A reduction in the in situ rates of oxygen and glucose consumption of cells in EMT6/Ro spheroids during growth. *Journal of Cellular Physiology* **124** (1985), No. 3, 516–524.
19. M. R. Gaddy et al., Optimization of spatiotemporally fractionated radiotherapy treatments with bounds on the achievable benefit. *Physics in Medicine & Biology* **63** (2018), No. 1, 015036.
20. M. R. Gaddy, J. Unkelbach, and D. Papp, Robust spatiotemporal fractionation schemes in the presence of patient setup uncertainty. *Medical Physics* **46** (2019), No. 7, 2988–3000.
21. J. M. P. C. Holash et al., Vessel cooption, regression, and growth in tumors mediated by angiopoietins and VEGF. *Science* **284** (1999), 1994–1998.
22. H. Iwata et al., Spot scanning and passive scattering proton therapy: Relative biological effectiveness and oxygen enhancement ratio in cultured cells. *International Journal of Radiation Oncology, Biology, Physics* **95** (2016), No. 1, 95–102.
23. R. K. Jain, R. T. Tong, and L. L. Munn, Effect of vascular normalization by antiangiogenic therapy on interstitial hypertension, peritumor edema, and lymphatic metastasis: insights from a mathematical model. *Cancer Research* **67** (2007), No. 6, 2729–2735.
24. M. C. Joiner and A. J. van der Kogel. *Basic Clinical Radiobiology*, CRC press, 2018.
25. P. Hahnfeldt et al., Tumor development under angiogenic signaling: a dynamical theory of tumor growth, treatment response, and postvascular dormancy. *Cancer Research* **59** (1999), No. 19, 4770–4775.
26. J. M. Kelm et al., VEGF profiling and angiogenesis in human microtissues. *Journal of Biotechnology* **118** (2005), No. 2, 213–229.
27. A. V. Kolobov and M. B. Kuznetsov, The study of angiogenesis effect on the growth rate of an invasive tumor using a mathematical model. *Russian Journal of Numerical Analysis and Mathematical Modelling* **28** (2013), No. 5, 471–484.
28. A. V. Kolobov, V. V. Gubernov, and M. B. Kuznetsov, The study of antitumor efficacy of bevacizumab antiangiogenic therapy using a mathematical model. *Russian Journal of Numerical Analysis and Mathematical Modelling* **30** (2015), No. 5, 289–298.
29. A. Köhn-Luque et al., Dynamics of VEGF matrix-retention in vascular network patterning. *Phys-*

ical Biology **10** (2013), No. 6, 066007.

30. M. B. Kuznetsov and A. V. Kolobov, Mathematical modelling of chemotherapy combined with bevacizumab. *Russian Journal of Numerical Analysis and Mathematical Modelling* **32** (2017), No. 5, 293–304.
31. M. B. Kuznetsov, V. V. Gubernov, and A. V. Kolobov, Analysis of anticancer efficiency of combined fractionated radiotherapy and antiangiogenic therapy via mathematical modelling – Analysis by mathematical modeling. *Russian Journal of Numerical Analysis and Mathematical Modelling* **33** (2018), No. 4, 225–242.
32. M. B. Kuznetsov and A. V. Kolobov, Transient alleviation of tumor hypoxia during first days of antiangiogenic therapy as a result of therapy-induced alterations in nutrient supply and tumor metabolism – Analysis by mathematical modeling. *Journal of Theoretical Biology* **451** (2018), 86–100.
33. M. Kuznetsov and A. Kolobov, Optimization of dose fractionation for radiotherapy of a solid tumor with account of oxygen effect and proliferative heterogeneity. *Mathematics* **8** (2020), No. 8, 1204.
34. M. Kuznetsov, J. Clairambault, and V. Volpert, Improving cancer treatments via dynamical biophysical models. *Physics of Life Reviews* **39** (2021), 1–48.
35. M. B. Kuznetsov and A. V. Kolobov, Spatial optimization of fractionated proton therapy via mathematical modeling. *Bulletin of the Lebedev Physics Institute* **49** (2022), No. 6, 174–179.
36. M. Kuznetsov and A. Kolobov, Optimization of antitumor radiotherapy fractionation via mathematical modeling with account of 4 Rs of radiobiology. *Journal of Theoretical Biology* **558** (2022), 111371.
37. M. Kuznetsov and A. Kolobov, Optimization of size of nanosensitizers for antitumor radiotherapy using mathematical modeling. *International Journal of Molecular Sciences* **24** (2023), No. 14, 11806.
38. A. Lorz et al., Modeling the effects of space structure and combination therapies on phenotypic heterogeneity and drug resistance in solid tumors. *Bulletin of Mathematical Biology* **77** (2015), No. 1, 1–22.
39. F. Mac Gabhann et al., Interactions of VEGF isoforms with VEGFR-1, VEGFR-2, and neuropilin in vivo: a computational model of human skeletal muscle. *American Journal of Physiology–Heart and Circulatory Physiology* **292** (2007), No. 1, H459–H474.
40. P. Mascheroni et al., Predicting the growth of glioblastoma multiforme spheroids using a multiphase porous media model. *Biomechanics and Modeling in Mechanobiology* **15** (2016), No. 5,1215–1228.
41. F. Michor and K. Beal, Improving cancer treatment via mathematical modeling: surmounting the challenges is worth the effort. *Cell* **163** (2015), No. 5, 1059–1063.
42. P. Netti et al., Role of extracellular matrix assembly in interstitial transport in solid tumors. *Cancer Research* **60** (2000), No. 9, 2497–2503.
43. S. F. Petit et al., Intra-voxel heterogeneity influences the dose prescription for dose-painting with radiotherapy: a modelling study. *Physics in Medicine & Biology* **54** (2009), No. 7, 2179.
44. R. N. Pittman, Regulation of tissue oxygenation. In: *Colloquium series on integrated systems physiology: from molecule to function*. Morgan & Claypool Life Sciences, 2011, pp. 1–100.
45. W. H. Press et al., *Numerical Recipes: The Art of Scientific Computing*, 3rd ed., Cambridge University Press, Cambridge, 2007.
46. R. S. Richardson et al., Human skeletal muscle intracellular oxygenation: the impact of ambient oxygen availability. *The Journal of Physiology* **571** (2006), No. 2, 415–424.

47. Å. Søvik et al., Optimization of tumour control probability in hypoxic tumours by radiation dose redistribution: a modelling study. *Physics in Medicine & Biology* **52** (2006), No. 2, 499.

48. S. K. Stamatelos et al., A bioimage informatics based reconstruction of breast tumor microvasculature with computational blood flow predictions. *Microvascular Research* **91** (2014), 8–21.

49. T. Stylianopoulos et al., Coevolution of solid stress and interstitial fluid pressure in tumors during progression: implications for vascular collapse evolution of solid and fluid stresses in tumors. *Cancer Research* **73** (2013), No. 13, 3833–3841.

50. V. V. Tuchin et al., In vivo investigation of the immersion-liquid-induced human skin clearing dynamics. *Technical Physics Letters* **27** (2001), No. 6, 489–490.

51. J. Unkelbach and D. Papp, The emergence of nonuniform spatiotemporal fractionation schemes within the standard BED model. *Medical Physics* **42** (2015), No. 5, 2234–2241.

52. J. Unkelbach et al., Spatiotemporal fractionation schemes for liver stereotactic body radiotherapy. *Radiotherapy and Oncology* **125** (2017), No. 2, 357–364.

53. P. Vera et al., Phase II study of a radiotherapy total dose increase in hypoxic lesions identified by 18F-misonidazole PET/CT in patients with non–small cell lung carcinoma (RTEP5 study). *Journal of Nuclear Medicine* **58** (2017), No. 7, 1045–1053.

54. S. Webb et al., A proof that uniform dose gives the greatest TCP for fixed integral dose in the planning target volume. *Physics in Medicine & Biology* **39** (1994), No. 11, 2091.

55. H. R. Withers, The four R's of radiotherapy. In: *Advances in Radiation Biology*, Elsevier, 1975, pp. 241–271.

56. H. R. Withers, J. M. G. Taylor, and B. Maciejewski, The hazard of accelerated tumor clonogen repopulation during radiotherapy. *Acta Oncologica* **27** (1988), No. 2, 131–146.

57. B. G. Wouters and J. M. Brown, Cells at intermediate oxygen levels can be more important than the 'hypoxic fraction' in determining tumor response to fractionated radiotherapy. *Radiation Research* **147** (1997), No. 5, 541–5502.

58. J. Wu, The enhanced permeability and retention (EPR) effect: The significance of the concept and methods to enhance its application. *Journal of Personalized Medicine* **11** (2021), No. 8, 771.

59. I. V. Zelepukin et al., Magnetometry based method for investigation of nanoparticle clearance from circulation in a liver perfusion model. *Nanotechnology* **30** (2019), No. 10, 105101.

60. L. Zhao et al., Radiosensitivity and relative biological effectiveness based on a generalized target model. *Journal of Radiation Research* **58** (2017), No. 1, 8–16.